Available online at www.sciencedirect.com
SCIENCE DIRECT
Journal of Volcanology and Geothermal Research 131 (2004) 397–410
Journal of volcanology and geothermal research
www.elsevier.com/locate/jvolgeores

Evidence for gas and magmatic sources beneath the Yellowstone volcanic field from seismic tomographic imaging

Stephan Husen *, Robert B. Smith, Gregory P. Waite

Department of Geology and Geophysics, University of Utah, Salt Lake City, UT, USA

Received 10 June 2003; accepted 20 November 2003

Abstract

The 3-D P-wave velocity and P- to S-wave velocity ratio structure of the Yellowstone volcanic field, Wyoming, has been determined from local earthquake tomography using new data from the permanent Yellowstone seismic network. We selected 3374 local earthquakes between 1995 and 2001 to invert for the 3-D P-wave velocity (V_p) and P-wave to S-wave velocity ratio (V_p/V_s) structure. V_p anomalies of small size (15×15 km) are reliably imaged in the northwestern part of the model outside the Yellowstone caldera; inside the caldera only V_p anomalies of large size extending over several grid nodes are reliably imaged. The V_p/V_s solution is generally poorer due to the low number of S–P arrival times. Only the northwestern part of the model is resolved with confidence; the V_p/V_s solution also suffers from strong vertical and horizontal velocity smearing. The tomographic images confirm the existence of a low V_p-body beneath the Yellowstone caldera at depths greater than 8 km, possibly representing hot, crystallizing magma. The most striking result of our study is a volume of anomalously low V_p and V_p/V_s in the northwestern part of the Yellowstone volcanic field at shallow depths of <2.0 km. Theoretical calculations of changes in P- to S-wave velocity ratios indicate that these anomalies can be interpreted as porous, gas-filled rock. The close spatial correlation of the observed anomalies and the occurrence of the largest earthquake swarm in historic time in Yellowstone, 1985, suggest that the gas may have originated as part of magmatic fluids released by crystallization of magma beneath the Yellowstone caldera.

Keywords: Yellowstone National Park; seismic tomography; 3-D velocity structure; magma chambers; carbon dioxide

1. Introduction

The Yellowstone volcanic field centered at the Yellowstone National Park, Wyoming, thereafter referred to as Yellowstone, is one of the largest and most active silicic volcanic systems in the world (Smith and Siegel, 2000; Christiansen, 2001). The youthful volcanic history of Yellowstone was dominated by three cataclysmic caldera-forming eruptions in the past two million years (Christiansen, 2001). The youngest eruption, at 0.64 million-years-old, formed the 40×60 km long Yellowstone caldera (Fig. 1). Since the last cataclysmic eruption at least 30 dominantly ryholitic and basaltic flows, as young as 70 000 years old, have been erupted, covering much of Yellowstone. Today, Yellowstone is still considered vol-

* Corresponding author. Present address: Swiss Seismological Service, ETH Hoenggerberg, CH 8093 Zurich, Switzerland. Fax: +41-1-445-1338.

E-mail address: husen@seismo.ifg.ethz.ch (S. Husen).

0377-0273/03/$ – see front matter © 2003 Elsevier B.V. All rights reserved.
doi:10.1016/S0377-0273(03)00416-5

canically active as indicated by its large hydrothermal system, its high seismicity, and episodes of caldera-wide deformation including uplift of up to 1 m from 1923 to 1984 followed by a rapid change to subsidence that exceeded 25 cm to 1995 followed again by uplift since 1995 (Pelton and Smith, 1979; Dzurisin et al., 1994; Wicks et al., 1998).

With over 10 000 geysers, hot springs, and fumaroles, Yellowstone has the world's highest concentration of hydrothermal features. Most of the active and recent hydrothermal features are within the 0.64-Ma Yellowstone caldera (Fig. 1). They are located either close to the outer edge of the main ring fracture zone forming the caldera or close to the margins of the resurgent domes, which formed after the last caldera forming eruption. The expansive hydrothermal system in Yellowstone is, in general, the result of hot water circulating along fracture systems in the upper crust heated from below by crystallizing magma (Fournier, 1989). Further evidence for a large body of crystallizing magma beneath Yellowstone comes from the extraordinarily high heat flux in Yellowstone. The combined conductive and convective heat flux at Yellowstone is estimated to be 1800 mW/m^2, which is 30 times the continental average (Fournier et al., 1976; Morgan et al., 1977).

Seismologically, crustal magma bodies are generally characterized by low P-wave velocities (V_p) and high P-wave to S-wave ratios (V_p/V_s). Previous local earthquake tomography studies at Yellowstone (Benz and Smith, 1984; Miller and Smith, 1999) imaged an extended body of low P-wave velocity (V_p) at depths of 6–12 km confirming the likely existence of crystallizing magma beneath the Yellowstone caldera. The previous studies, however, used limited earthquake data up to 1994 and very little S-wave data owing to the small number of three-component seismometers in Yellowstone at that time. Nonetheless, due to the sensitivity of V_p/V_s to changes in pore fluids (Ito et al., 1979; Mavko and Mukerji, 1995) it is an important parameter to image and detect fluids in volcanic systems.

In this study, we extend the work by Benz and Smith (1984) and Miller and Smith (1999) to image the crustal structure beneath Yellowstone. Since 1995 significant technical upgrades and expansion of the permanent seismic network at Yellowstone have increased the number of three-component stations to six (Fig. 1) providing more S-wave data than the previous studies. We selected 3374 local earthquakes between 1995 and 2001, providing 34 538 P-wave times and 5875 S–P arrival times, to image the 3-D V_p and V_p/V_s structure of the upper crust beneath Yellowstone by local earthquake tomography. Solution quality of our tomographic model is assessed by analyzing the resolution matrix and tests with synthetic data. Our new results imaged the same low V_p-body beneath the Yellowstone caldera detected in previous studies. The most striking new result of this study is a shallow body of low V_p and low V_p/V_s beneath the northwestern part of Yellowstone. Theoretical modeling of V_p/V_s ratios suggests that this seismic anomaly can be caused by the existence of gas. The close spatial correlation of the seismic anomalies and the occurrence of the largest historic earthquake swarm in Yellowstone further suggest that the gas may have originated as part of a volcanic fluid system released by crystallization of magma beneath the Yellowstone caldera.

2. Local earthquake data

Yellowstone is the most seismically active region of the 1300-km-long Intermountain Seismic Belt (Smith and Arabasz, 1991) that extends from northern Montana to northern Arizona providing an excellent source for local earthquake tomography studies (Fig. 1). Seismicity in Yellowstone is routinely observed at a permanent seismic network. Since 1984, seismic data in Yellowstone have been acquired, analyzed, and archived at the University of Utah Seismograph Stations (UUSS) (Nava and Smith, 1996). This study uses data from 1995 to 2001 recorded at nineteen, one-component, short-period seismometers and six, three-component seismometers, two of which were broadband seismometers (Fig. 2). The dataset was augmented by data collected at a temporary deployment of broadband seismometers be-

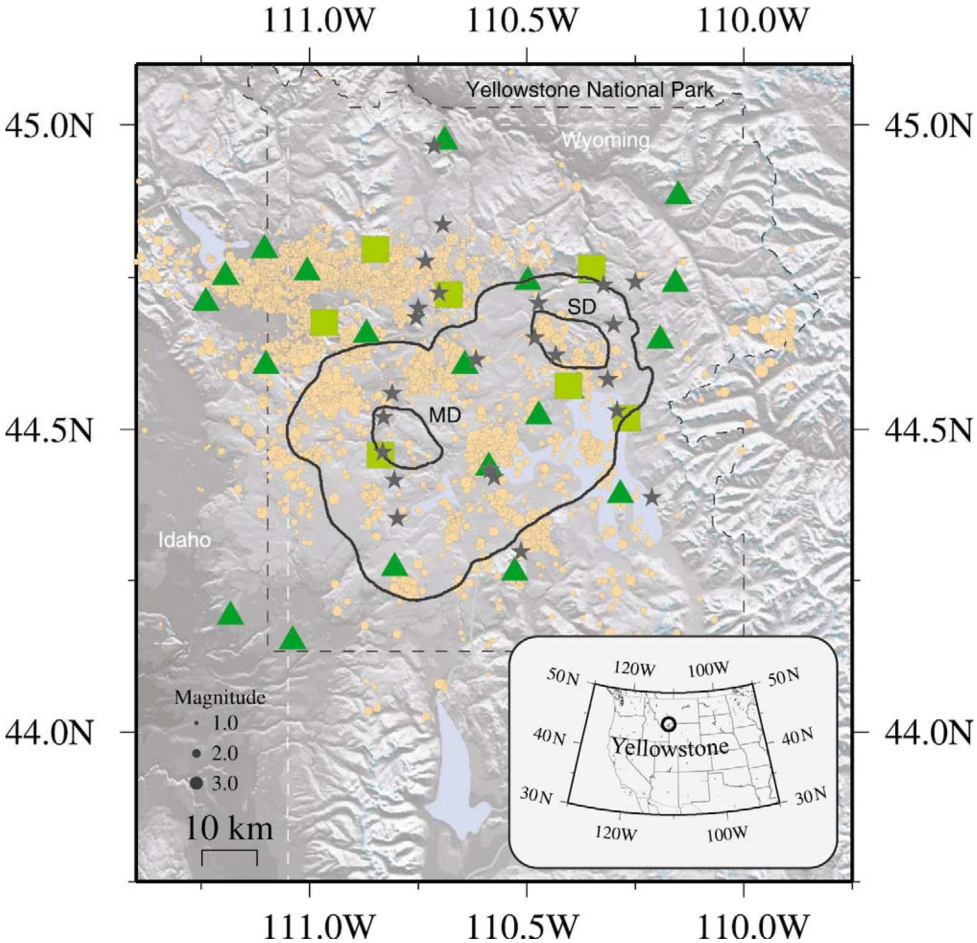

Fig. 1. Map of the Yellowstone area showing hypocenter locations between 1995 and 2001 (orange circles), seismic stations of the permanent network (green triangles and squares), and mapped hydrothermal features (black stars). Hypocenter locations are scaled by magnitude as indicated. Black lines outline the 0.64-Ma caldera boundary and location of the Mallard Lake (MD) and Sour Creek (CD) resurgent domes. Dashed black line marks boundary of the Yellowstone National Park; dashed gray lines mark state boundaries. Inset map shows location of the Yellowstone area in the US.

tween late 1990 and early 1994 to gather all available S-wave data (Miller and Smith, 1999).

P-wave arrivals are routinely picked at the UUSS for all events; S-wave arrivals, however, are only routinely picked if they show a clear onset. We increased the number of available S-wave arrivals by 20% by repicking events with a local coda magnitude (M_c) > 1.0. S-wave arrivals were only taken from horizontal components of the three-component seismometers to reduce the potential of picking precursors such as P to S converted phases instead of the S-wave arrival. Picking of S-wave arrivals at stations inside the caldera was notably difficult; only a few clear arrivals could be determined for these stations. Both, P- and S-wave arrivals are weighted applying a 0, 1, 2, 3 scheme corresponding to a picking uncertainty interval of 0.06 s, 0.12 s, 0.30 s, and 0.60 s, respectively. A weight of zero is applied to arrivals with the lowest uncertainty (0.06 s). To account for the lower precision of S-wave arrivals, the highest weight assigned by the UUSS for a S-wave arrival is 2.

Due to coupling of seismic velocities and hypocenter locations, local earthquake tomography demands a careful selection of earthquake data to be used in the inversion. We inverted a subset of 482 high-quality earthquakes for a minimum 1-D model (Kissling et al., 1994) that includes P- and S-wave velocities and station delays. Prior to selection for the 3-D inversion, all earthquakes were relocated using the obtained minimum 1-D model. We finally selected 3374 earthquakes (Fig. 2), applying the following selection criteria: (1) at least 7 P-wave arrivals and 1 S-wave arrival, (2) at least one observation within 1.5 focal depth distance, and (3) an azimuthal gap $< 180°$. The second constraint is required to provide good control over focal depth since hypocenter locations with no observations at nearby stations show large uncertainties in focal depth (Husen et al., 2003). The final data set consisted of 34 538 P-arrival times and 5875 S–P arrival times. Estimated picking uncertainty is 0.15 s for the combined data set.

The spatial distribution of selected earthquakes is strongly heterogeneous (Fig. 2). Most of the earthquakes are located in the northwest close to the Hebgen Lake area, MT, just outside the Yellowstone caldera. Seismicity within the caldera

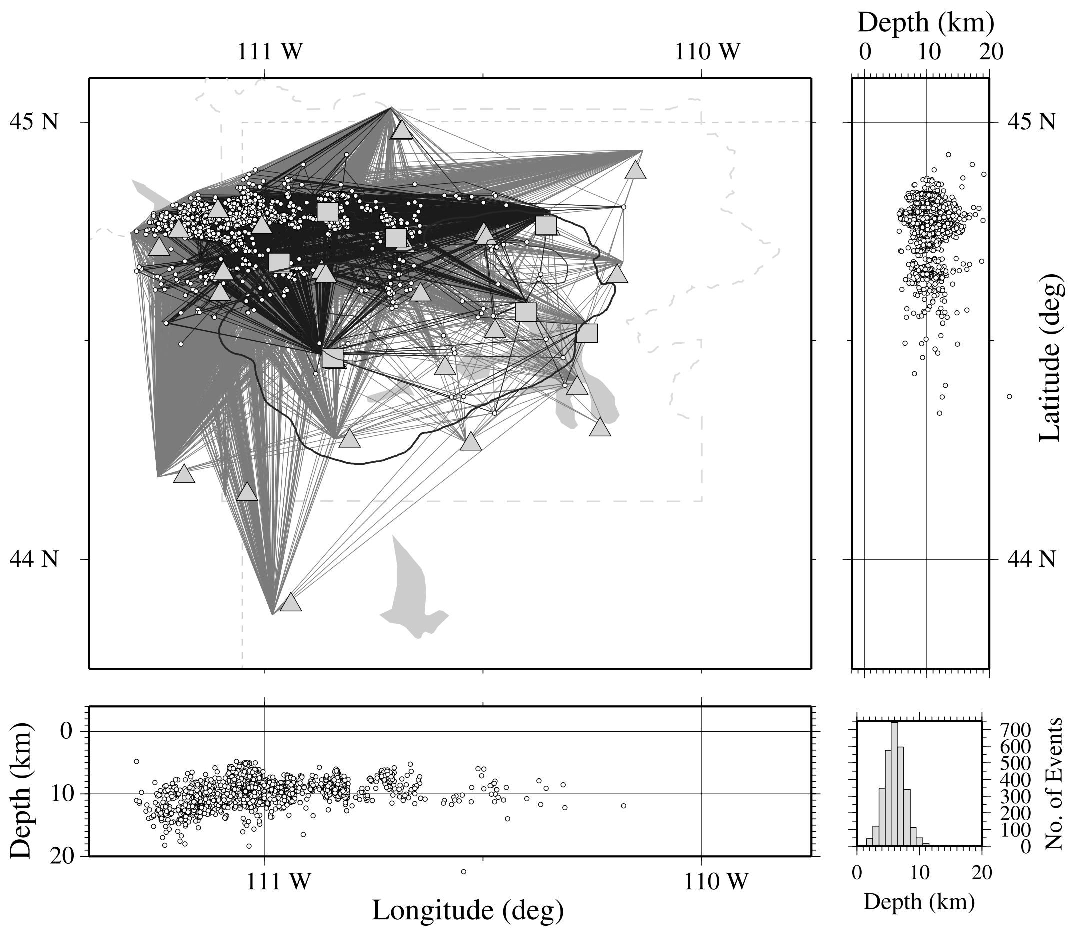

Fig. 2. Hypocenter locations selected for tomographic inversion of this study. 2-D P-wave and S-wave ray coverage is shown by gray and black lines, respectively. Hypocenter locations are shown in map view and vertical cross sections in E–W and N–S direction. Grey triangles and squares mark one-component and three-component seismic stations, respectively. Black lines mark outline of the 0.64-Ma caldera boundary and resurgent domes. Lower right shows histogram of focal depth distribution of selected hypocenter locations.

is usually very shallow (0–4 km depth) requiring a station within short distance for those earthquakes to be included in the tomographic inversion. Consequently, a large portion of the seismicity within the caldera could not be used in this study due to the relatively sparse distribution of seismic stations. Ray coverage of P-wave arrivals is dense to the northwest of the Yellowstone caldera and within the northern part of the Yellowstone caldera (Fig. 2); lack of seismicity and sparser station distribution yield poor ray coverage in the southern and eastern part of the Yellowstone caldera. The ratio between P- and S-wave arrivals is very poor because of the low number of three-component stations and the difficulties in picking precise S-arrivals at station in the southeastern part of the caldera. Hence, good S-wave ray coverage is restricted to the northwestern part of the study area (Fig. 2). The heterogeneous ray coverage of P- and S-wave arrivals will require a very careful analysis of the solution quality of the tomographic model.

3. Method

We used the computer code simulps14 (Thurber, 1983; Eberhart-Phillips, 1990), extended by Haslinger and Kissling (Haslinger and Kissling, 2001) for full 3-D ray shooting, to invert simultaneously for hypocenter locations and 3-D velocity structure (V_p and V_p/V_s). The method inverts S–P arrival times for V_p/V_s by projecting S–P arrival time residuals into V_p/V_s variations (Thurber and Atre, 1993). S- and P-arrival time residuals are computed by 3-D ray tracing through the corresponding velocity models; the necessary S-wave velocity model is derived from the V_p and V_p/V_s models. The inversion for V_p/V_s is preferable because V_p/V_s (or equivalently Poisson's ratio) is an important parameter to infer fluid content and mechanical rock properties. Furthermore, direct comparison of 3-D P- and S-velocity models to infer the 3-D V_p/V_s structure is hampered by the tendency for S-velocity models to be more poorly resolved than the P-velocity models (Eberhart-

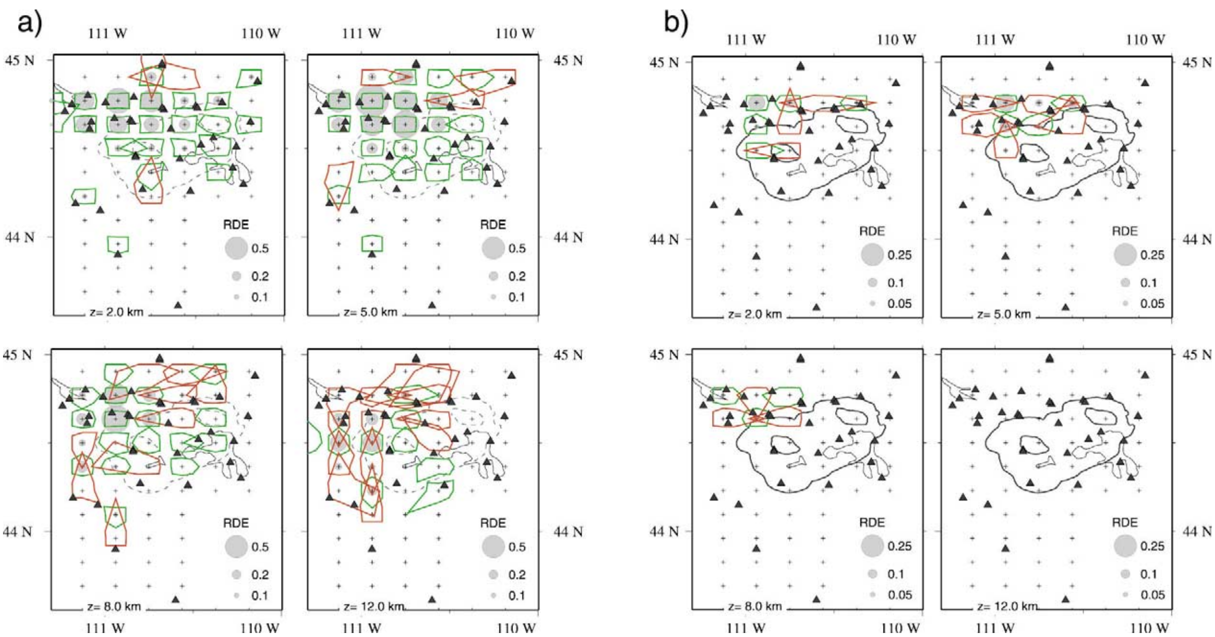

Fig. 3. Diagonal elements of the resolution matrix (RDE) and resolution contours (Reyners et al., 1999) of the (a) V_p and (b) V_p/V_s solution at different depths. RDE are shown as scaled gray circles. Note different scaling for (a) and (b). Contour lines denote the area in which the values of the resolution matrix decay to 70% of the value of the RDE; green and red red contour lines denote gird nodes with no and significant velocity smearing, respectively. Black triangles mark seismic stations.

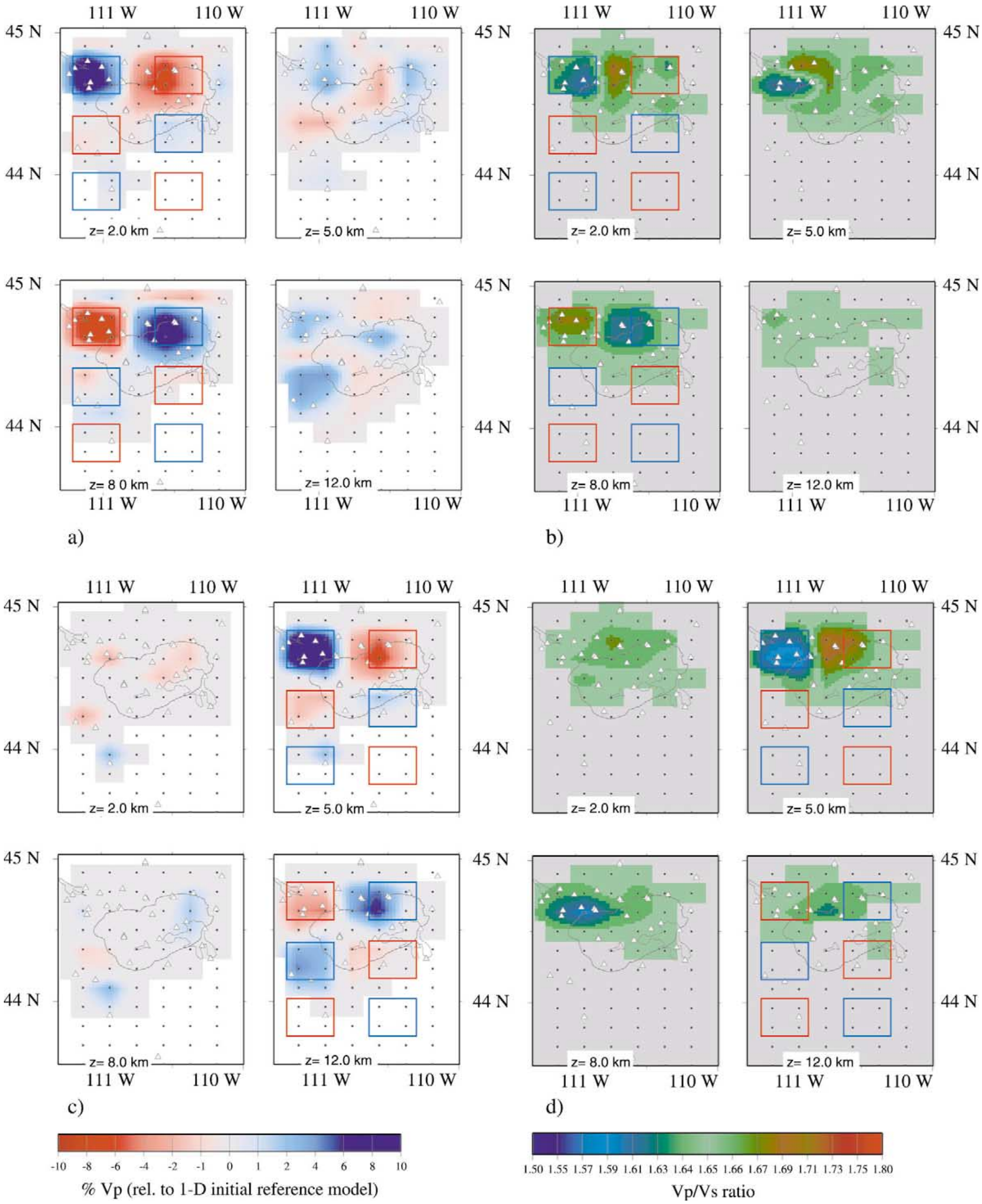

Fig. 4. Assessing solution quality of (a,c) V_p and (b,d) V_p/V_s model using synthetic checkerboard models. Recovered model after five iterations is shown in plane view at different depths. Locations of high (+10%) and low (−10%) V_p input anomalies are shown by blue and red squares, respectively; locations of high (1.73) and low (1.57) V_p/V_s input anomalies are shown by red and blue squares, respectively. Solid squares mark individual grid nodes of the model parameterization; white triangles mark seismic stations

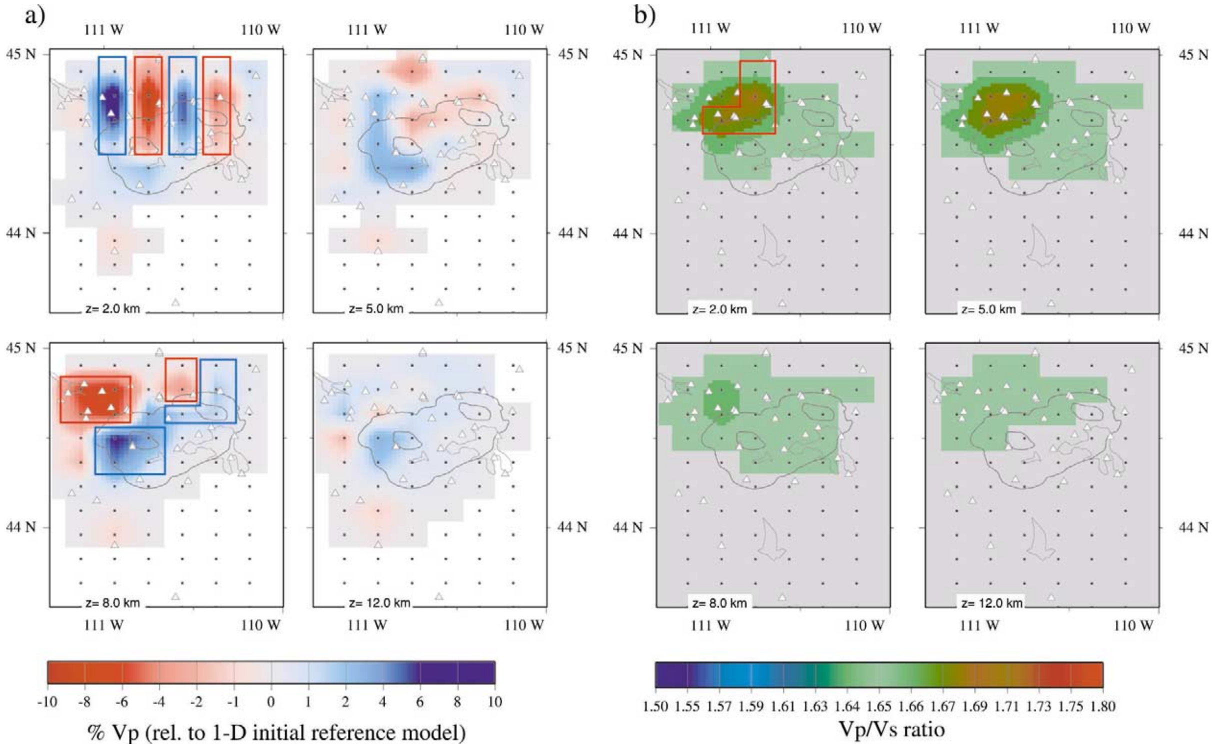

Fig. 5. Assessing solution quality of (a) V_p and (b) V_p/V_s model using synthetic characteristic models. See text for explanation of characteristic model. Recovered model after five iterations is shown in plane view at different depths. Locations of high (+10%) and low (−10%) V_p input anomalies are shown by blue and red squares, respectively; locations of high (1.73) and low (1.57) V_p/V_s input anomalies are shown by red and blue squares, respectively. Solid squares mark individual grid nodes of the model parameterization; white triangles mark seismic stations.

Phillips, 1990). This effect becomes important if the number of S-wave arrivals is much lower than the number of P-wave arrivals as in our study – 34 538 P vs. 5875 S–P arrival times.

Simulps14 solves the non-linear, coupled hypocenter-velocity problem by a linearized, iterative, damped least-square scheme. Each iteration consists of an inversion for V_p and V_p/V_s variations and for hypocenter locations. After each iteration new ray paths and new travel time residuals are computed using the updated velocity models. Damping values were selected to be 500 for V_p and V_p/V_s by analyzing trade-off curves between model variance and data variance (Eberhart-Phillips, 1986). The chosen damping values provided the largest reduction in data variance without increasing model variance strongly, hence yielding the smoothest solution to fit the data.

Assessing the correct model parameterization in seismic tomography is a difficult task since solution and solution quality are strongly affected by the chosen model parameterization (Kissling et al., 2001). In simulps14 velocity models are defined by grid nodes with linear interpolation in between using the same grid nodes for V_p and V_p/V_s. We used tests with synthetic data and different model parameterizations to find the most appropriate model parameterization. Final grid node spacing was 15×15 km in horizontal direction; grid nodes in vertical direction were positioned at −4.0 (above sea level), −1.0, 2.0 (below sea level), 5.0, 8.0, 12.0, 16.0, and 21.0 km. The high number of P-wave arrivals would support finer grid spacing for the V_p model, in particular in the northwestern part of the model, but the low number of S–P arrivals did not. It would be possible to invert first for the V_p model using a finer model parameterization, and subsequently invert

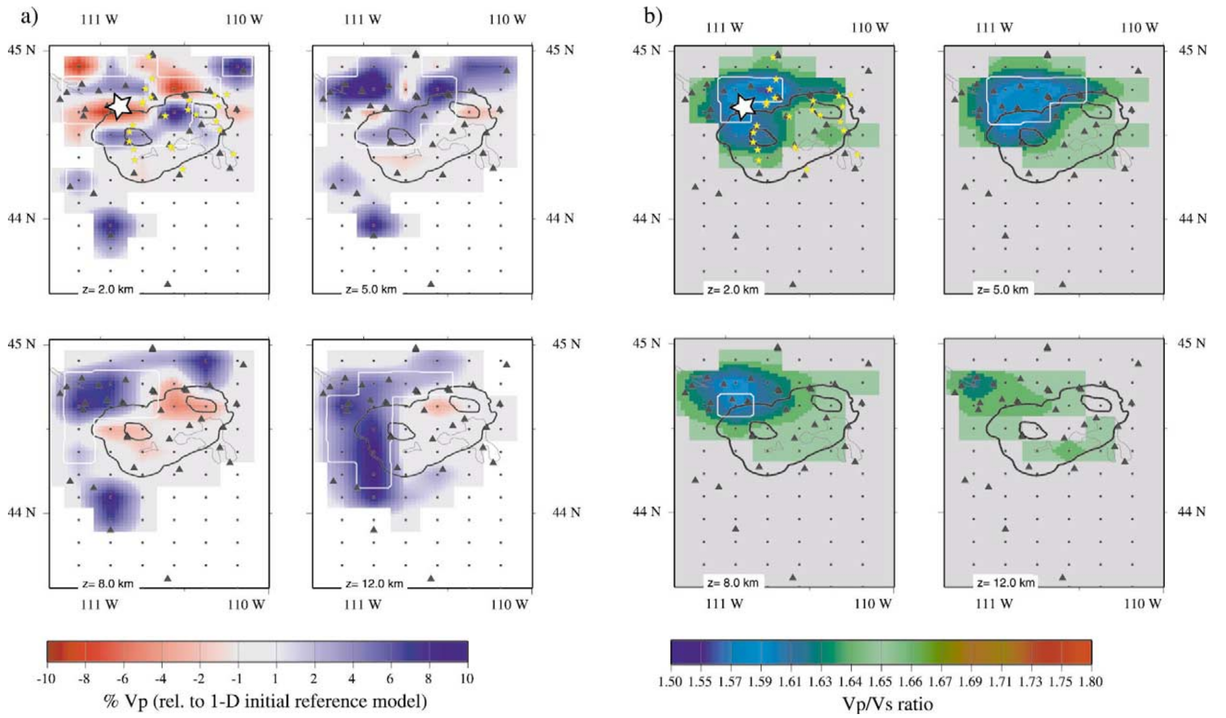

Fig. 6. Tomographic results of 3-D (a) V_p and (b) V_p/V_s models. Results are in horizontal cross sections at different depths as indicated. V_p velocity structure is shown as percentage change relative to 1-D initial reference model. V_p/V_s velocity structure is shown as absolute V_p/V_s ratios; initial V_p/V_s ratio was 1.65. Areas with no ray coverage are masked. White triangles mark stations used in the inversion. White lines contours areas of RDE > 0.05; black lines outline 0.64-Ma caldera boundary and location of resurgent domes, respectively. Yellow stars mark mapped hydrothermal features (Christiansen, 2001) and large white star marks location of the 1985 earthquake swarm (Waite and Smith, 2002).

for the coarser V_p/V_s model by interpolating and fixing V_p on the coarser model. Since we are interested in interpreting V_p and V_p/V_s together, this procedure would complicate the interpretation unnecessarily.

Linearization of the non-linear, coupled hypocenter-velocity problem demands initial velocities and hypocenter locations to be close to their true values. We chose the minimum 1-D V_p model as described above as initial reference model for the V_p inversion since it has been proven to be the most appropriate initial reference model in local earthquake tomography (Kissling et al., 1994). A constant V_p/V_s of 1.65 determined by Wadati diagrams was used as initial estimate for the V_p/V_s model. Solving for V_p/V_s makes the assumption

Table 1
Theoretical changes in V_p/V_s ratios computed from $V_p/V_s = [K_{eff}/\mu_{eff}]^{1/2}$

Type of change	Porosity			
	0 (%)	0.02 (%)	0.05 (%)	0.1 (%)
Pore fluid: Liquid → gas	0	−0.6	−1.8	−8.0
ΔT = +100°C (liquid/gas)	0%/0%	−0.6/0	−0.6/0	−1.7/0
ΔP = +50 Mpa (liquid/gas)	0/0	0/0.6	0/0.6	1.0/5.0

The effective bulk and shear modulus were computed using Gasmann's relations (Gassmann, 1951). For changes in temperature and pressure the corresponding changes for a liquid and gaseous pore fluid are given. See text for more details.

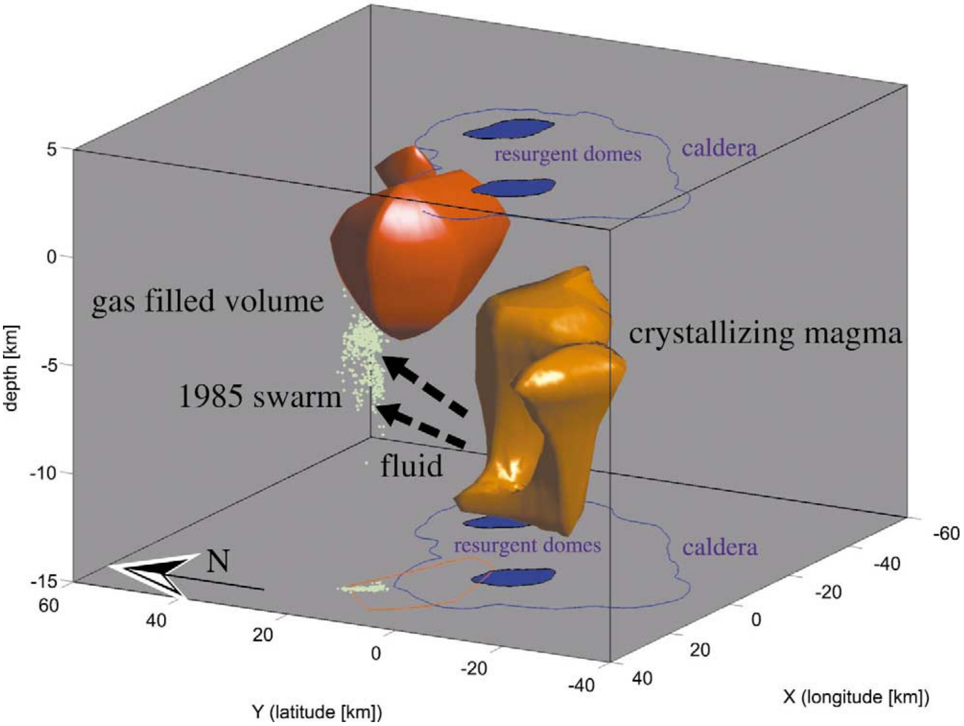

Fig. 7. 3-D view of low V_p beneath Yellowstone as imaged by local earthquake tomography in this study. Orange body outlines location of a possible crystallizing magma body beneath the Yellowstone caldera; red body outlines location of shallow, possible gas filled volume. Light green dots are hypocenter locations of the 1985 swarm. Dashed arrows denote possible fluid migration from the crystallizing magma body towards gas filled volume thereby causing 1985 swarm activity. At lower plane of the 3-D cube red line contours extend of the gas filled volume at 2.0 km depth; green dots are hypocenter locations of 1985 swarm.

that, given a heterogeneous V_p model and unknown V_s, it is more reasonable to estimate V_s from the V_p model using a constant V_p/V_s than to assume a homogeneous 1-D V_s model (Eberhart-Phillips and Reyners, 1997).

4. Solution quality

Heterogeneous distribution of source and receivers requires careful assessment of the solution quality in seismic tomography, i.e. defining areas of reliable solution and detecting possible artifacts. In general, the solution quality of a certain volume or model parameter depends mainly on the geometric distribution and density of rays (ray coverage). Plotting resolution estimates such as hit count, diagonal elements of the resolution matrix (RDE), and spread function are common ways to assess ray coverage (see e.g. Reyners et al., 1999; Husen et al., 2000). RDE and resolution contours for the V_p and V_p/V_s solution are shown in Fig. 3. Resolution contours try to visualize possible velocity smearing in 2-D, i.e. the dependency of the solution of one model parameter on its neighbors (Reyners et al., 1999). RDE are relatively high (>0.5) and horizontal smearing is small for the V_p solution in the northwestern part of the model (Fig. 3); within the Yellowstone caldera RDE decrease rapidly and some significant smearing becomes visible. Due to the low number of S–P arrival times, RDE of the V_p/V_s solution are significant smaller in the northwestern part of the model; the area inside the Yellowstone is not resolved at all. Some horizontal smearing is present even in the densest northwestern part of the V_p/V_s model.

Resolution estimates depend strongly on the chosen damping and model parameterization degrading the usefulness of resolution estimates to assess the solution quality. Tests with synthetic data are therefore indispensable to define areas of good and low resolution. These tests usually involve the construction of synthetic input velocity models and computation of synthetic travel times using the source receiver distribution of the real data set. Checkerboards (Humphreys and Clayton, 1988; Zelt, 1998) or spikes (Spakman and Nolet, 1988) are common synthetic input models to assess the amount of image blurring in a data set. We constructed two checkerboard models (Fig. 4): each consisted of alternating high and low anomalies spanning over two grid nodes in x- and y-direction; between the anomalies one grid node was left open to test for horizontal velocity smearing. Amplitudes of the input anomalies were $\pm 10\%$ and 1.57/1.73 for the V_p and V_p/V_s model, respectively. The first checkerboard model (Fig. 4a,b) had anomalies placed at 2.0 and 8.0 km depth; in the second model (Fig. 4c,d) anomalies were placed at 5.0 and 12.0 km depth. Contrary to regular checkerboard models, layers in between were left open to test for vertical smearing.

As can be inferred from Fig. 4a,c resolution of the northwestern part of the V_p model is good at all depths; only minor vertical smearing is detected between 2.0 and 5.0 km depth. The northeastern part of the Yellowstone caldera is also well resolved in the V_p model at all depths with some horizontal smearing towards the west. The southern part of the caldera shows strongly decreased amplitudes of the input anomalies but the checkerboard pattern is still discernible at 5.0 and 12.0 km depth. Recovery of the V_p/V_s checkerboard model is much poorer. Only the northwestern part of the model is resolved with strong smearing between 2.0 and 5.0 km and between 5.0 and 8.0 km depth (Fig. 4b,c). There is also strong horizontal smearing at 2.0, 5.0, and 8 km depth, which resulted in a shifted position of the recovered anomalies (Fig. 4b,d).

Checkerboard tests or spike sensitivity tests as described above cannot be used to assess the power of the data to resolve a certain structure. The ability of the data to resolve a fine-scale structure such as a checkerboard does not imply that large-scale structures can be resolved as well (Leveque et al., 1993). Following Haslinger (1999) and Husen et al. (2000), we designed a synthetic input model, called the characteristic model, that is based on the inversion results obtained with 'real' data. A characteristic model retains the sizes and amplitudes (characteristics) of anomalies seen in the inversion results but has rotated shapes and different signs for the anomalies. Our characteristic model (Fig. 5) has velocity anomalies at 2.0 and 8.0 km depth since these layers showed the strongest anomalies after the inversion. Recovery of the input structure is good for the V_p model although amplitudes at 8 km depth in the eastern part of the model are strongly decreased (Fig. 5a). Recovery of the V_p/V_s input structure is fair with strongly decreased amplitudes and strong vertical smearing is visible. Note, how the structure changed its shape at 5.0 km, which is clearly an effect of horizontal and vertical smearing.

5. Tomographic results

After five iterations, our final tomographic model for Yellowstone achieved a data variance reduction of 62% and 77% for the 3-D V_p and the V_p/V_s solution, respectively; weighted data root-mean-square (RMS) misfit of the combined model was 0.12 s, which is in the order of a priori picking uncertainty. The V_p and V_p/V_s images reveal several significant features (Fig. 6). At shallow depth (2.0 km) a strong low V_p anomaly (-10% relative to the initial 1-D reference model) is located in the northwestern part of the model close to the caldera boundary. A similar low V_p anomaly is located further to the east just north of the caldera boundary. Absolute velocities of both anomalies are as low as 4.6 km/s. Based on our tests with synthetic data both anomalies are well resolved. A third strong low V_p anomaly in the northwest corner of the model is likely to be an artifact of the inversion due to low resolution in this area. The V_p/V_s model shows a large low V_p/V_s anomaly in the northwestern part of the model close to the caldera boundary (Fig. 6). Absolute V_p/V_s is as low as 1.57, which corresponds to a

−5% change compared to the initial value of 1.65. Due to the inherent vertical smearing and image blurring we cannot distinguish if the anomaly is located at 2.0 or 5.0 km depth. The close spatial correlation of the V_p/V_s anomaly with the strong low V_p anomaly, however, suggests that the V_p/V_s anomaly actually locates at 2.0 km depth. This is further constrained by our test with the characteristic model (Fig. 5), which placed an anomaly at 2.0 km depth and showed similar smearing as in the 'real' tomographic images.

Large, low V_p anomalies (−6% relative to the initial 1-D reference model) are observed inside the Yellowstone caldera at depths greater than 8 km (Fig. 6). Absolute V_p is as low as 5.4 km/s at 8 km depth. Because of degrading resolution at 12 km depth we cannot resolve if these low V_p anomalies continue to greater depth. The tomographic images suggest two isolated V_p anomalies focussed beneath the two resurgent domes (Fig. 6). Little horizontal smearing in this area (Fig. 3) would confirm this interpretation although general resolution is only fair (Figs. 4 and 5). Unfortunately, poor resolution of the V_p/V_s model inhibits any information on V_p/V_s inside the Yellowstone caldera.

6. Discussion

At 8 km depth our V_p model is in good agreement with previously published velocity models for Yellowstone (Benz and Smith, 1984; Miller and Smith, 1999). These studies interpreted caldera wide low V_p as caused by increased rock temperature due to the presence of a crystallizing magma body. High V_p surrounding the Yellowstone caldera (Fig. 6) was interpreted as thermally undisturbed basement and sedimentary rocks (Miller and Smith, 1999). Because our V_p/V_s model does not resolve this part of the caldera we can neither confirm nor disagree on the existence of a crystallizing magma body beneath the Yellowstone caldera at depths ≥ 8.0 km. Given the volcanic history of Yellowstone and the existence of a widespread hydrothermal system, it is likely to expect crystallizing magma beneath the Yellowstone caldera. The lack of clear S-arrivals at stations in the southeastern part of the caldera, even for events of sufficient large magnitude, may be caused by high attenuation as the waves travel through areas of elevated temperature. A similar effect has been observed in the Andes for seismic waves traveling through the active magmatic arc (Haberland and Rietbrock, 2001).

Our new result is the detection of a strong low V_p and V_p/V_s anomaly at 2 km depth in the northwestern part of the model close to the caldera boundary (Fig. 6). Seismic velocities and V_p/V_s are sensitive to changes in pore-fluid content, temperature, and pore pressure (Ito et al., 1979; Mavko and Mukerji, 1995). For solid rock a theoretical V_p/V_s can be computed as:

$$\frac{V_p}{V_s} = \left[\frac{K_{\mathrm{eff}}}{\mu_{\mathrm{eff}}} + \frac{4}{3}\right]^{1/2} \tag{1}$$

where K_{eff} and μ_{eff} are the effective bulk and shear moduli, respectively. The effective bulk and shear moduli depend on rock matrix, pore fluid content, porosity, pore pressure, and temperature. In the presence of fluids, effective bulk and shear moduli can be computed by Gassman's equations (Gassmann, 1951):

$$\frac{K_{\mathrm{eff}}}{K_0 - K_{\mathrm{eff}}} = \frac{K_{\mathrm{dry}}}{K_0 - K_{\mathrm{dry}}} + \frac{K_{\mathrm{fl}}}{\phi(K_0 - K_{\mathrm{fl}})}, \quad \mu_{\mathrm{eff}} = \mu_{\mathrm{dry}} \tag{2}$$

where K_{dry} and μ_{dry} are the effective moduli of dry rock, K_{fl} is the effective bulk modulus of pore fluid, K_0 is the bulk modulus of mineral material making up the rock matrix, and ϕ is porosity. Gassman's equations assume statistical isotropy of the pore space but are free of assumptions of pore geometry. They are, however, only valid for sufficiently low frequencies such that pore pressures are equilibrated throughout the pore space. This is usually fulfilled for low seismic frequencies (<100 Hz). We can apply the relatively simple Gassman's equations because we only interpret changes in V_p/V_s (in percent) due to changes in the pore fluid. Absolute values of V_p/V_s are strongly decreased as demonstrated by tests with synthetic data in Section 5.

Using the empirical concept of critical porosity ϕ_c (Nur et al., 1995), K_{dry} and μ_{dry} (in Eq. 2) can be expressed as:

$$\left.\begin{aligned} K_{dry} &= K_0\left(1-\frac{\phi}{\phi_c}\right) \\ \mu_{dry} &= \mu_0\left(1-\frac{\phi}{\phi_c}\right) \end{aligned}\right\}, \text{ for } \phi < \phi_c. \tag{3}$$

Table 1 lists theoretical changes in V_p/V_s ratios due to changes in pore fluid, temperature, and pore pressure computed using Eqs. 1–3. We assumed a rock matrix of 60% quartz and 40% alkali feldspar. Bulk moduli of liquid (H_20) and gas (CO_2) were taken from fig. 14 of Batzle and Wang (1992) and computed using eqs. 9–11 of Batzle and Wang (1992), respectively. Results from Batzle and Wang (1992) are based on conditions typically encountered in oil exploration. Their approximations, however, are adequate as long as pseudoreduced pressure and temperature are not both within about 0.1 of unity (Batzle and Wang, 1992). For Yellowstone, these conditions are met for temperature and pressure conditions of 150°C and 50 MPa at 2 km depth, assuming a conductive temperature gradient and hydrostatic pore pressure. A critical porosity ϕ_c of 0.15 was assumed based on a similar study in Iceland (Miller et al., 1998).

As inferred from Table 1, a change in pore fluid from liquid to gas produces a significant decrease in V_p/V_s for high porosities. A porosity of 10% causes a decrease of 8% in V_p/V_s that is close to what we observe in the tomographic images. The effect of increasing temperature on V_p/V_s is always smaller than that for a change in pore fluid. An increase in pore pressure causes a positive change in V_p/V_s for high porosities, which is contrary to what we observe in the tomographic images. The strong decrease in V_p/V_s for a change in pore fluid from liquid to gas is caused by the very low bulk modulus of gas, which is several magnitudes smaller than the bulk modulus of liquids. Consequently, the presence of gas should not be only indicated by a negative V_p/V_s anomaly but also by a strong negative V_p anomaly as we observed it in our tomographic results.

Earlier work in Yellowstone indicated low V_p/V_s caused by the presence of hot water at temperatures and pore pressures near the water–steam transition (Chatterjee et al., 1985), but these were restricted to a few hydrothermally active areas of Yellowstone. Areas of low V_p/V_s were observed and interpreted as caused by gaseous pore fluid in other geothermal and volcanic environments, including The Geysers, CA (Julian et al., 1996) and Long Valley, CA (Julian et al., 1998). The decrease in V_p/V_s was interpreted to be caused by steam in The Geysers and CO_2 in Long Valley. Although Yellowstone has extensive hydrothermal activity (Fournier, 1989), no hydrothermal features are mapped in the area of the observed low V_p and V_p/V_s anomalies (Fig. 6) excluding steam as a possible gas. On the other hand, cooling of a large magmatic body beneath Yellowstone would release a significant amount of magmatic fluids including both liquids and gas (Fournier, 1989, 1999). CO_2 is a major component of magmatic fluids and isotopic signatures of soil CO_2 in the Mud Volcano area in the center of the Yellowstone caldera suggest a deep origin (Werner et al., 2000). These fluids may occasionally migrate outward from the Yellowstone caldera, perhaps inducing earthquake swarms such as the large 1985 earthquake swarm (Waite and Smith, 2002), which was located directly beneath the observed V_p and V_p/V_s anomalies (Figs. 6 and 7).

The depth of the V_p and V_p/V_s anomalies at 2 km suggests a model in which CO_2 could migrate upwards towards the surface. Unfortunately, no data on soil CO_2 is available in this area due to its remoteness and associated logistic difficulties. Large emissions of CO_2 at the surface can result in significant tree killing due to increased soil CO_2 concentrations as it has been observed at Mammoth Mountain, Long Valley, CA (Farrar et al., 1995). Unfortunately, a large wildfire in 1988 burned most of the northwestern part of the Yellowstone region erasing any potential evidence of trees killed by CO_2.

It is tempting to interpret the second anomaly of low V_p to the east and north of the caldera boundary (Fig. 6) as evidence for another gas filled body. However, V_p/V_s in this area is not resolved. Furthermore, this negative V_p anomaly locates close to the Norris–Mammoth corridor, a deep graben bounded to the west by the Gallatin fault. It is filled with low-velocity alluvium and colluvium, which were imaged as well in previous seismic studies (Benz and Smith, 1984; Miller and Smith, 1999).

7. Summary and conclusions

We have tomographically imaged the 3-D V_p and V_p/V_s structure beneath the Yellowstone volcanic field (Figs. 6 and 7). The low number of three-component seismometers, however, limited the number of available S–P arrival times, and thus good resolution of the V_p/V_s model is confined to the shallow upper crust in the northwestern part of the Yellowstone caldera. The tomographic images confirm the existence of a large body of low V_p at depths greater than 8 km beneath the Yellowstone caldera. Based on previous results, this body may represent crystallizing magma. Our new result is the detection of a low V_p and a low V_p/V_s anomaly in the shallow crust of the northwestern part of Yellowstone. Computed changes in V_p/V_s ratios indicate that this anomaly can be modeled as a change in pore fluid from liquid to gas – likely CO_2 – at shallow crustal depths. The close spatial correlation of the observed V_p and V_p/V_s anomalies with the location of the 1985 earthquake swarm suggests a model in which CO_2 as part of magmatic fluids exsolved from a large crystallizing magma body beneath the Yellowstone caldera and occasionally migrated outwards of the Yellowstone caldera (Fig. 7). Our results show a strong similarity with volcanic processes at the Long Valley Caldera, CA, where CO_2 emissions killed trees following a large earthquake swarm in 1989 (Farrar et al., 1995; Hill et al., 1990). The results further suggest that the release of magmatic fluids at greater depth and their subsequent accumulation at shallow depth are important volcanic processes that may pose a risk to human safety.

Acknowledgements

We thank the University of Utah Seismograph Station staff, in particular Sue Nava, Jeff Fotheringham, Dave Drobeck, and Ken Whipp, for assistance with data acquisition and analyses. Incorporated Research Institutions in Seismology provided broadband seismographs for two winters of temporary deployment. We also thank the National Park Service for their cooperation in earthquake and GPS monitoring in Yellowstone. We appreciate thoughtful comments by David Hill, Bruce Julian, Jake Lowenstern, and Gary Mavko. We thank Claudio Chiarabba and Saturo Tanaka for their thoughtful and constructive reviews. This research was funded by the Swiss Science Foundation (Grant 8220-061284) and by the US Geological Survey Cooperative Agreement #01HQAG0008 for support of the Yellowstone seismic and GPS networks under the Yellowstone Volcano Observatory. Support was also provided by the NSF Continental Dynamics Program (Grant Collaborative Research 'Geodynamics of the Yellowstone Hotspot from Seismic and GPS Imaging', award #9725431).

References

Batzle, M., Wang, Z., 1992. Seismic properties of pore fluids. Geophysics 57, 1396–1408.

Benz, H.M., Smith, R.B., 1984. Simultaneous inversion for lateral velocity variations and hypocenters in the Yellowstone region using earthquake and refraction data. J. Geophys. Res. 89, 1208–1220.

Chatterjee, S.N., Pitt, A.M., Iyer, H.M., 1985. V_p/V_s ratios in the Yellowstone National Park region, Wyoming. J. Volcanol. Geotherm. Res. 26, 213–230.

Christiansen, R.L., 2001. The Quaternary and Pliocene Yellowstone plateau Volcanic field of Wyoming, Idaho, and Montana. US Geological Survey 729-G.

Dzurisin, D., Yamashita, K.M., Kleinman, J.W., 1994. Mechanisms of crustal uplift and subsidence at the Yellowstone caldera, Wyoming. Bull. Volcanol. 56, 261–270.

Eberhart-Phillips, D., 1986. Three-dimensional velocity structure in northern California Coast Range from inversion of local earthquake arrival times. Bull. Seismol. Soc. Am. 76, 1025–1052.

Eberhart-Phillips, D., 1990. Three-dimensional P and S velocity structure in the Coalinga Region, California. J. Geophys. Res. 95, 15343–15363.

Eberhart-Phillips, D., Reyners, M., 1997. Continental subduction and three-dimensional crustal structure: The northern South Island, New Zealand. J. Geophys. Res. 102 (B6), 11843–11861.

Farrar, C.D. et al., 1995. Forest-killing diffuse CO_2 emission at Mammoth Mountain as a sign of magmatic unrest. Nature 376, 675–678.

Fournier, R.O., 1989. Geochemistry and dynamics of the Yellowstone National Park hydrothermal system. Ann. Rev. Earth Planet. Sci. 17, 13–53.

Fournier, R.O., 1999. Hydrothermal processes related to movement of fluid from plastic into brittle rock in magmatic–epithermal enviroment. Econ. Geol. 94, 1193–1210.

Fournier, R.O., White, D.E., Truesdell, A.H., 1976. Convective heat flow in Yellowstone National Park. Second United Nations Symposium on Development and Use of Geothermal Resources. US Goverment Printing Office, Washington, DC, pp. 731–739.

Gassmann, F., 1951. Ueber die Elastizitaet poroeser Medien. Vier. der Natur. Ges. Zuerich 96, 1–23.

Haberland, C., Rietbrock, A., 2001. Attenuation tomography in the western central Andes: A detailed insight into the structure of a magmatic arc. J. Geophys. Res. 106 (B6), 11151–11167.

Haslinger, F., Kissling, E., 2001. Investigating effects of 3-D ray tracing methods in local earthquake tomography. Phys. Earth Planet. Int. 123, 103–114.

Haslinger, F., et al., 1999. 3D crustal structure from local earthquake tomography around Gulf of Arta (Ionian region, NW Greece). Tectonophysics 304, 210–218.

Hill, D.P. et al., 1990. The 1989 earthquake swarm beneath Mammoth Mountain, California: An initial look at the 4 May through 30 September activity. Bull. Seismol. Soc. Am. 80, 325–339.

Humphreys, E., Clayton, R.W., 1988. Adapation of back projection tomography to seismic travel time problems. J. Geophys. Res. 93, 1073–1085.

Husen, S., et al., 2003. Probabilistic earthquake location in complex 3-D velocity models: Application to Switzerland. J. Geophys. Res. 108(B2) (doi:10.1029/2002JB001778).

Husen, S., Kissling, E., Flueh, E.R., 2000. Local earthquake tomography of shallow subduction in north Chile: A combined onshore and offshore study. J. Geophys. Res. 105, 28183–28198.

Ito, H., DeVilbiss, J., Nur, A., 1979. Compressional and shear waves in saturated rock during water-steam transition. J. Geophys. Res. 84, 4731–4735.

Julian, B.R., Pitt, A.M., Foulger, G.R., 1998. Seismic image of a CO_2 reservoir beneath a seismically active volcano. Geophys. J. Int. 133, F7–F10.

Julian, B.R., Ross, A., Foulger, G.R., Evans, J.R., 1996. Three-dimensional seismic image of a geothermal reservoir: The Geysers, California. Geophys. Res. Lett. 23, 685–688.

Kissling, E., Ellsworth, W.L., Eberhart-Phillips, D., Kradolfer, U., 1994. Initial reference models in local earthquake tomography. J. Geophys. Res. 99, 19635–19646.

Kissling, E., Husen, S., Haslinger, F., 2001. Model parameterization in seismic tomography: A choice of consequences for the solution quality. Phys. Earth Planet. Int. 123, 89–101.

Leveque, J.-J., Rivera, L., Wittlinger, G., 1993. On the use of the checkerboard test to assess the resolution of tomographic inversions. Geophys. J. Int. 115, 313–318.

Mavko, G., Mukerji, T., 1995. Seismic pore space compressibility and Gassman's relation. Geophysics 60, 1743–1749.

Miller, A.D., Julian, B.R., Foulger, G.R., 1998. Three-dimensional seismic structure and moment tensors of non-double-couple earthquakes at the Hengill–Grensdalur volcanic complex, Iceland. Geophys. J. Int. 133, 309–325.

Miller, D.S., Smith, R.B., 1999. P and S velocity structure of the Yellowstone volcanic field from local earthquake and controlled-source tomography. J. Geophys. Res. 104 (B7), 15105–15121.

Morgan, P., Blackwell, D.D., Spafford, R.E., Smith, R.B., 1977. Heat flow measurements in Yellowstone Lake and the thermal structure of the Yellowstone Caldera. J. Geophys. Res. 82, 3719–3732.

Nava, S.J., Smith, R.B., 1996. Earthquake catalog for the Yellowstone National Park region, January 1, 1992 to December 31, 1994, with a contribution by R. A. Hutchinson: Summary of felt earthquakes in Yellowstone National Park, 1992–1994. Univ. of Utah Seismogr. Stn., Salt Lake City.

Nur, A., Mavko, G., Dvorkin, J., Gal, D., 1995. Critical porosity: The key to relating physical properties to porosity in rocks. Proc. 65th Ann. Int. Meeting. Soc. Expl. Geophys., 878 pp.

Pelton, J.R., Smith, R.B., 1979. Recent crustal uplift in the Yellowstone National Park. Science 206, 1179–1182.

Reyners, M., Eberhart-Phillips, D., Stuart, G., 1999. A three-dimensional image of the shallow subduction: Crustal structure of the Raukumara Peninsula, New Zealand. Geophys. J. Int. 137, 873–890.

Smith, R.B., Arabasz, W.J., 1991. Seismicity of the Intermountain Seismic Belt. In: Slemmons, D.B., Engdahl, E.R., Zoback, M.L., Blackwell, D.D. (Eds.), Neotectonics of North America. Geol. Soc. Am., Boulder, CO, pp. 185–228.

Smith, R.B., Siegel, L., 2000. Windows into the Earth: The Geology of Yellowstone and Grand Teton Parks. Oxford University Press, 247 pp.

Spakman, W., Nolet, G., 1988. Imaging algorithms, accuracy and resolution in delay time tomography. In: Vlaar, N.J., Nolet, G., Wortel, M.J.R., Cloething, S.A.P.L. (Eds.), Mathematical Geophysics. Reidel, Dordrecht, pp. 155–187.

Thurber, C.H., 1983. Earthquake locations and three-dimensional crustal structure in the Coyote Lake area, central California. J. Geophys. Res. 88, 8226–8236.

Thurber, C.H., Atre, S.R., 1993. Three-dimensional V_p/V_s variations along the Loma Prieta rupture zone. Bull. Seismol. Soc. Am. 83, 717–736.

Waite, G.P., Smith, R.B., 2002. Seismic evidence for fluid migration accompanying subsidence of the Yellowstone caldera. J. Geophys. Res. 107(B9) (doi: 10.1029/2001JB000586).

Werner, C., Brantley, S.L., Boomer, K., 2000. CO_2 emissions related to the Yellowstone volcanic system 2. Statistical sampling, total degassing, and transport mechanisms. J. Geophys. Res. 105 (B5), 10831–10846.

Wicks, J.R., Thatcher, W., Dzurisin, D., 1998. Migration of fluids beneath Yellowstone caldera inferred from Satellite radar interferometry. Science 282, 458–462.

Zelt, C.A., 1998. Lateral velocity resolution from three-dimensional seismic refraction data. Geophys. J. Int. 135, 1101–1112.